Simulations of ENSO Phase-Locking in CMIP5 and CMIP6®

HAN-CHING CHEN^a AND FEI-FEI JIN^a

^a Department of Atmospheric Sciences, University of Hawai'i at Mānoa, Honolulu, Hawaii

(Manuscript received 13 November 2020, in final form 15 March 2021)

ABSTRACT: The characteristics of El Niño–Southern Oscillation (ENSO) phase-locking in observations and CMIP5 and CMIP6 models are examined in this study. Two metrics based on the peaking month histogram for all El Niño and La Niña events are adopted to delineate the basic features of ENSO phase-locking in terms of the preferred calendar month and strength of this preference. It turns out that most models are poor at simulating the ENSO phase-locking, either showing little peak strength or peaking at the wrong seasons. By deriving ENSO's linear dynamics based on the conceptual recharge oscillator (RO) framework through the seasonal linear inverse model (sLIM) approach, various simulated phase-locking behaviors of CMIP models are systematically investigated in comparison with observations. In observations, phase-locking is mainly attributed to the seasonal modulation of ENSO's SST growth rate. In contrast, in a significant portion of CMIP models, phase-locking is codetermined by the seasonal modulations of both SST growth and phase transition rates. Further study of the joint effects of SST growth and phase transition rates suggests that for simulating realistic winter peak ENSO phase-locking with the right dynamics, climate models need to have four key factors in the right combination: 1) correct phase of SST growth rate modulation peaking at the fall, 2) large-enough amplitude for the annual cycle in growth rate, 3) small amplitude of semiannual cycle in growth rate, and 4) small amplitude of seasonal modulation in SST phase transition rate.

KEYWORDS: Dynamics; ENSO; Sea surface temperature; Thermocline; Climate models; Interannual variability; Seasonal cycle

1. Introduction

El Niño-Southern Oscillation (ENSO) is the dominant climate mode of interannual variability in the tropical Pacific with significant global impacts. ENSO events usually occur during boreal spring and summer, reach their peak in boreal winter, and then decay in the spring of the second year. This feature of preferred peak timing, known as the phase-locking phenomenon, is still an active subject in ENSO research. Two possible phase-locking mechanisms have been proposed by previous studies: 1) the linear mechanism (i.e., the seasonal modulation of ENSO instability; Philander et al. 1984; Hirst 1986; An and Wang 2001; Burgers 2005) and 2) the nonlinear mechanism (i.e., the nonlinear interaction between inherent ENSO cycle and annual cycle; Jin et al. 1994; Tziperman et al. 1994). Using a conceptual recharge oscillator (RO) model, Chen and Jin (2020) investigated these two mechanisms in both unforced and stochastic forcing scenarios and found that the difference in phase-locking performance between the nonlinear and linear mechanisms will be largely smoothed out in the presence of noise forcing. Stein et al. (2010, 2014) and Chen and Jin (2020) further demonstrated that ENSO phase-locking is mainly dominated by the seasonal modulation of ENSO instability. In Chen and Jin (2020), they proved that the RO model, which only considers the linear dynamics of ENSO, can reproduce the

Corresponding author: Fei-Fei Jin, jff@hawaii.edu

found that ENSO phase-locking was not adequately simulated by most CGCMs (Joseph and Nigam 2006; Wittenberg et al. 2006; Ham et al. 2013). It remains unclear why most models fail to simulate phase-locking of ENSO to boreal winter. Zheng and Yu (2007) linked the boreal summer ENSO phase-locking in the CGCM to its double ITCZ bias. Ham et al. (2013) found

large SST gradient and the thermocline shoaling in the boreal summer, which enhanced the zonal advection feedback and thermocline feedback. Ham and Kug (2014) also obtained similar results for a set of CMIP3 and CMIP5 models. Rashid

that ENSO's summer peak in the GFDL CGCM is due to the

main phase-locking features found in observations. The preferred calendar month of ENSO peak time mainly depends on

the phase and amplitude of the seasonal modulation of the SST

growth rate. In addition, the strength of the phase-locking

preference is controlled by the seasonal mean of SST growth

The intensity of the coupled instability, which is responsible

for the evolution of ENSO, varies seasonally. Several factors

could cause strong instability, including high sea surface tem-

perature (SST), location of the intertropical convergence zone

(ITCZ) near the equator (Philander 1983), and strong equa-

torial zonal surface wind, which is accompanied by a large

mean SST gradient, shallow thermocline, and strong upwelling

(Battisti 1988). Together these factors make the instability

strongest during boreal summer to autumn (Philander 1983;

Tziperman et al. 1997), leading to the ENSO events reaching

their peak during boreal winter (Li 1997; Chen and Jin 2020).

Even with these advances in qualitative understanding the

mechanism of ENSO phase-locking, which controls the phase-

locking of ENSO in coupled ocean-atmosphere general cir-

culation models (CGCMs), is still inconclusive. Several studies

rate and its seasonal modulation amplitude.

DOI: 10.1175/JCLI-D-20-0874.1

[©] Supplemental information related to this paper is available at the Journals Online website: https://doi.org/10.1175/JCLI-D-20-0874.s1.

and Hirst (2016) found that incorrect simulation of shortwave feedback and thermocline feedback caused the wrong peak month of ENSO phase-locking in the ACCESS model. Several studies also argued that phase-locking is sensitive to shortwave feedback (Bellenger et al. 2014; Wengel et al. 2018).

The strong preference for the phase-locking with both El Niño and La Niña peaking during the winter season is a fundamental observed feature of ENSO. The poor simulations in CMIP models imply that these climate models do not sufficiently capture the seasonal modulation of ENSO linear dynamics. A better understanding of the dynamics of ENSO phase-locking may lead to improved ENSO simulations in CGCMs. Moreover, it is essential to have realistic ENSO phase-locking in climate models for ENSO prediction skill (Jin and Kinter 2009). Improved simulations of phase-locking by climate models may improve the skill of ENSO predictions. We conduct a systematic evaluation of the current CMIP5 and CMIP6 models in terms of each model's linear dynamics for ENSO phase-locking. By deriving the linear ENSO dynamics based on the conceptual RO framework, various state-of-the-art climate models are investigated and compared with observations.

This paper is arranged as follows. Section 2 introduces observational datasets, climate models, and the methodology applied in this study. Section 3 discusses the features of ENSO phase-locking in observations, CMIP models, and linear RO model simulations using the parameters obtained from the seasonal linear inverse model (sLIM). By deriving ENSO's linear dynamics using the conceptual RO framework through the sLIM approach, various simulated phase-locking behaviors of CMIP models are systematically investigated and compared with observations in section 4. In section 5, the sensitivity examination using the linear RO model is conducted to investigate the joint effects of SST growth and phase transition rates in climate models. Section 6 gives a summary and discussion.

2. Data and method

a. The recharge oscillator model

The linear stochastic RO model (Jin 1997a,b; Burgers et al. 2005) can almost perfectly simulate the ENSO phase-locking features when forced by artificial noise forcing, which is consistent with the view that ENSO phase-locking is mainly attributed to the seasonal modulation of linear dynamics and the nonlinearity is nonessential (Chen and Jin 2020). Therefore, we only consider the linear dynamics of RO model as follows:

$$\frac{dT}{dt} = RT + F_1 h + \sigma_T \xi_T \,, \tag{1}$$

$$\frac{dh}{dt} = -rh - F_2 T + \sigma_h \xi_h , \qquad (2)$$

$$\frac{d\xi_T}{dt} = -m_T \xi_T + w_T(t) , \qquad (3)$$

$$\frac{d\xi_h}{dt} = -m_h \xi_h + w_h(t) , \qquad (4)$$

where T and h are the area-averaged eastern equatorial Pacific SST anomalies (5°S–5°N, 150°–90°W) and western equatorial Pacific

thermocline anomalies (5°S-5°N, 120°E-155°W), respectively. The selection of the T and h regions is based on the first mode of empirical orthogonal function (EOF) analysis of SST anomalies and associated thermocline anomalies, respectively. In observations and most CMIP models, there are significant SST anomalies in the Niño-3 region and related thermocline anomalies over 5°S-5°N, 120°E-155°W (not shown). The terms R and r are the growth rate, and F_1 and F_2 are the phase transition rate; σ_T and σ_h are the noise amplitude, $w_T(t)$ and $w_h(t)$ are independent white noise term, and ξ_T and ξ_h are normalized Gaussian distributed red noise with a decay time scale of $1/m_T$ and $1/m_h$, respectively. The choice of parameters is determined from the observations and CMIP models using the seasonal linear inverse model (sLIM). The amplitude of noise (σ_T and σ_h) is estimated as the standard deviation of the residual from the RO system after sLIM. All RO simulations include the mean value of parameters. All the simulated results are from the last 20 000 years of the 21 000-yr model run with a 5-day time step.

b. The seasonal linear inverse model

The linear inverse model (LIM; Penland and Sardeshmukh 1995) method has been widely used for exploring the dynamics of ENSO (Vimont et al. 2014; Newman et al. 2009, 2011; Penland and Sardeshmukh 1995). Here we consider the following dynamics system:

$$\frac{d\mathbf{X}}{dt} = \mathcal{L}(t)\mathbf{X} + \xi. \tag{5}$$

This system can be used as a linear approximation for the dynamics of observed $\mathbf{X}(t)$ with the \mathcal{L} operator and noise ξ . In the Earth climate system, the seasonal cycle is one of the critical components of the climate background in addition to climate mean state. Thus, it is often essential to consider the seasonal cycle in the linear operator \mathcal{L} :

$$\mathcal{L} = \mathcal{L}_0 + \mathcal{L}_a \,, \tag{6}$$

where \mathcal{L}_0 and \mathcal{L}_a indicate the mean and seasonal cycle of the \mathcal{L} operator, respectively. However, including a seasonal cycle into \mathcal{L} means the degrees of freedom increase significantly and often require much more data. For example, if $\mathcal{L}(t)$ is examined using a monthly time interval, 12 matrices are needed to resolve the annual cycle of \mathcal{L} into a monthly time scale. Here, we propose an approximate approach, called the seasonal linear inverse model (sLIM), to consider the modulations of seasonal cycles without increasing degrees of freedom. Let us consider the following approximation for the linear and annual periodic operator:

$$\mathcal{L}_{a} = \mathcal{L}_{1}^{c} \cos(\omega t) + \mathcal{L}_{1}^{s} \sin(\omega t) + \mathcal{L}_{2}^{c} \cos(2\omega t) + \mathcal{L}_{2}^{s} \sin(2\omega t) + \mathcal{L}_{3}^{c} \cos(3\omega t) + \mathcal{L}_{3}^{s} \sin(3\omega t) + \dots,$$
(7)

where $\omega = 2\pi/(12 \text{ months})$. By applying a perturbation method, the subsequent solution \mathcal{L} operator is expanded as $\mathcal{L} = \mathcal{L}^{(0)} + \mathcal{L}^{(1)} + \mathcal{L}^{(2)} + \dots$ The details of our procedures are described in the appendix. This general method can be applied to ENSO or other elements, such as the MJO. Because the

TABLE 1. List of 47 CMIP5 models and 43 CMIP6 models analyzed in this study.

No.	CMIP5	No.	CMIP6
1	ACCESS1.0	48	ACCESS-CM2
2	ACCESS1.3	49	ACCESS-ESM1-5
3	BCC-CSM1.1	50	AWI-CM-1-1-MR
4	BCC-CSM1.1-M	51	AWI-ESM-1-1-LR
5	BNU-ESM	52	BCC-CSM2-MR
6	CanESM2	53	BCC-ESM1
7	CCSM4	54	CAMS-CSM1-0
8	CESM1-BGC	55	CAS-ESM2-0
9	CESM1-CAM5	56	CESM2
10	CESM1-CAM5.1-FV2	57	CESM2-FV2
11	CESM1-FASTCHEM	58	CESM2-WACCM
12	CESM1-WACCM	59	CESM2-WACCM-FV
13	CMCC-CESM	60	CIESM
14	CMCC-CM	61	CMCC-CM2-SR5
15	CMCC-CMS	62	CanESM5
16	CNRM-CM5	63	E3SM-1-0
17	CNRM-CM5.2	64	E3SM-1-1
18	CSIRO-Mk3.6.0	65	E3SM-1-1-ECA
19	EC-EARTH	66	EC-Earth3
20	FGOALS-g2	67	EC-Earth3-Veg
21	FGOALS-s2	68	EC-Earth3-Veg-LR
22	FIO-ESM	69	FGOALS-f3-L
23	GFDL-CM2p1	70	FGOALS-g3
24	GFDL CM3	71	FIO-ESM-2-0
25	GFDL-ESM2G	72	GFDL-CM4
26	GFDL-ESM2M	73	GISS-E2-1-G
27	GISS-E2-H	74	GISS-E2-1-G-CC
28	GISS-E2-H-CC	75	GISS-E2-1-H
29	GISS-E2-R	76	INM-CM4-8
30	GISS-E2-R-CC	77	INM-CM5-0
31	HadGEM2-AO	78	IPSL-CM6A-LR
32	HadCM3	79	MCM-UA-1-0
33	HadGEM2-CC	80	MIROC6
34	HadGEM2-ES	81	MPI-ESM-1-2-HAM
35	IPSL-CM5A-LR	82	MPI-ESM1-2-HR
36	IPSL-CM5A-MR	83	MPI-ESM1-2-LR
37	IPSL-CM5B-LR	84	MRI-ESM2-0
38	MIROC-ESM	85	NESM3
39	MIROC-ESM-CHEM	86	NorCPM1
40	MIROC5	87	NorESM2-LM
41	MPI-ESM-MR	88	NorESM2-MM
42	MPI-ESM-LR	89	SAM0-UNICON
42	MPI-ESM-LK MPI-ESM-P	90	TaiESM1
43 44	MRI-CGCM3	90	1 dIL SIVII
45	MRI-ESM1		
45 46	NorESM1-M		
47	NorESM1-ME		
4/	NOIESWII-ME		

ENSO system's seasonal modulation beyond the semiannual cycle is so weak, we only consider the mean state, annual cycle, and semiannual cycle in this study. Compared to the conventional method, which estimates the annual cycle of $\mathcal L$ based on each calendar month, sLIM can obtain the mean and seasonal cycle of the $\mathcal L$ operator with limited data. In this study, the state vector $\mathbf X$ is defined as

$$\mathbf{X} = \begin{bmatrix} T \\ h \end{bmatrix},\tag{8}$$

where T and h are the interpolated pentad (5-day) areaaveraged eastern equatorial Pacific SST anomalies and western equatorial Pacific thermocline anomalies, respectively, as defined in Eqs. (1) and (2).

c. Observations and CMIP models

The observed SST used in this study is the monthly Hadley Centre Global Sea Ice and Sea Surface Temperature dataset (HadISST; Rayner et al. 2003). The thermocline depth (D20) is obtained from the Simple Ocean Data Assimilation (SODA) reanalysis, version 2.2.4 (Giese and Ray 2011). We assess simulated ENSO behavior of phase-locking in CGCMs taking part in phases 5 and 6 of the Coupled Model Intercomparison Project [CMIP5 (Taylor et al. 2012) and CMIP6 (Eyring et al. 2016)]. The monthly SST and D20 are from 47 CMIP5 and 43 CMIP6 models historical simulations (models are listed in Table 1). Only one ensemble member for each model is used (e.g., the r1i1p1 integration for CMIP5 and r1i1p1f1 for CMIP6). Each historical simulation was integrated from a preindustrial control simulation spinup experiment and then forced by solar, volcanic, aerosol, and greenhouse gas data from 1850 to 2005 for the CMIP5 historical experiments and from 1850 to 2014 for the CMIP6 historical experiments.

In this study, we analyze all the observed and simulated output from 1871 to 2005 to coincide with the period of observations and CMIP dataset. The anomalies here are based on the climatology from 1871 to 2005 and are detrended by subtracting the linear trend. The El Niño (La Niña) events in the observations and models are defined as occurring when the 3-month running averaged Niño-3 index is greater than 1.0 standard deviations (less than -1.0 standard deviation).

d. Metrics of ENSO phase-locking

The seasonal variance of SST anomaly and phase histogram of SST anomaly peak time accounting to the calendar month are two commonly used measures for the ENSO phase-locking. Although both methods can capture the preferred peak month of ENSO phase-locking, only the peak phase histogram measure correctly describes the strength of phase-locking and the asymmetry of phase-locking between El Niño and La Niña (Chen and Jin 2020). The calendar month of the ENSO peak is defined as the maximum (minimum) peak of a 3-month running-averaged Niño-3 index within a 10-month time window to avoid double peaks in a single El Niño (La Niña) event. In this study, the 3-month smoothed histogram of ENSO peak phase is used to characterize phase-locking behaviors. Two metrics of ENSO phase-locking are adopted here to delineate the basic phase-locking features in terms of the most preferred peak month and strength of its preference. The metric of the preferred calendar month of phase-locking (φ_p) is defined as the calendar month at which histogram has its maximum peak. The metric for the strength of ENSO's phase-locking preference (φ_s) is defined as

$$\varphi_s = \frac{4}{3} \left(\varphi_{\text{max}} - \frac{1}{4} \right), \tag{9}$$

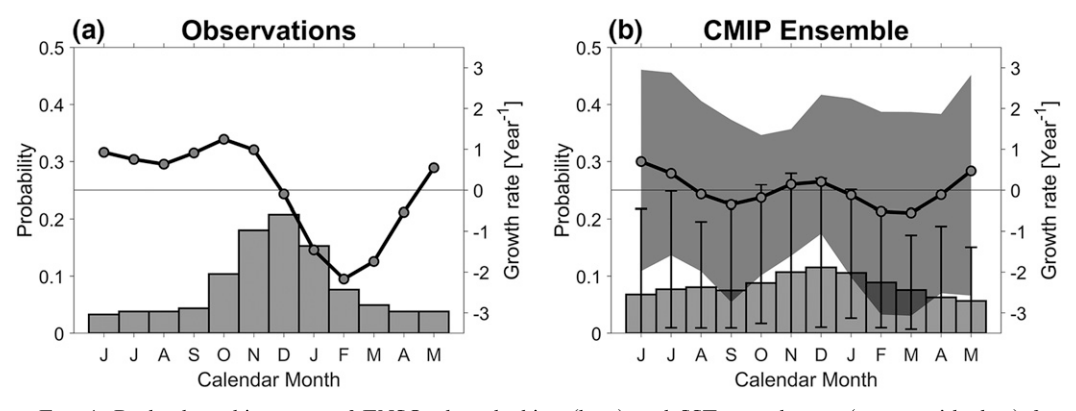


FIG. 1. Peak phase histogram of ENSO phase-locking (bars) and SST growth rate (curves with dots) for (a) observations and (b) ensemble mean of CMIP5 and CMIP6 models. The vertical lines and shading in (b) indicate the minimum and maximum values of the histogram and growth rate, respectively. The mean of SST growth rate is removed.

where $\varphi_{\rm max}$ indicates the sum of the 3-month highest values of the histogram centered on φ_p . The value of φ_s is between 0 and 1, where 0 indicates no locking and 1 complete locking within a 3-month window. Chen and Jin (2020) defined a metric of sharpness of the histogram to evaluate the strength of phase-locking preference and it is highly correlated with the metric of phase-locking strength φ_s ; however, it is easier and more straightforward to evaluate the strength of phase-locking preference using φ_s .

3. Features of ENSO phase-locking in observations and CMIP models

a. Observations and CMIP models

In observations, ENSO events have a strong preference for phase-locking and its preferred peak times tend to occur toward the end of the calendar year from November to January, where the seasonal cycle of ENSO's SST growth rate (R)transitions from positive to negative (Fig. 1a). However, most climate models fail to simulate ENSO phase-locking and seasonal modulation of R (Fig. 1b and SFig. 1 in the online supplemental material). Moreover, in observations, the seasonal modulation of R is dominated by the annual cycle and the semiannual component is much smaller; while in many climate models, the modulation of R has a strong semiannual cycle and plays a secondary role against the annual cycle (SFig. 1). According to the preferred peak month φ_p , climate models simulated diverse peak calendar month for ENSO phaselocking, and only about one-third of the models simulate ENSO peaking in boreal winter (Figs. 2a,b). For the strength of phase-locking preference φ_s , most models are weak compared with observations (Figs. 2c,d). It is not surprising that there is only a weak phase-locking preference in CMIP5 and CMIP6 ensemble (Fig. 1b) and the seasonal variation of R is also weak in many models (SFig. 1). The failure of the climate models' simulation of ENSO phase-locking raises the question of why models are doing so poorly and what controls ENSO's phaselocking.

b. Linear RO model simulations

As the observed properties of ENSO phase-locking can be simulated in a linear RO model (Chen and Jin 2020), we first use the sLIM approach to derive the linear dynamics of ENSO [Eqs. (1) and (2)] and then force the RO model by an artificially generated noise forcing [Eqs. (3) and (4)]. This linear stochastic model does a good job of reproducing the ENSO phase-locking for observations (Fig. 3a) and CMIP models (Fig. 3e and SFig. 2). Three sensitivity RO simulations are considered here to examine the effects of the seasonal modulation of RO parameter: 1) both seasonal modulations of SST growth rate and phase transition rates are considered (RO-T), 2) seasonal modulation of SST growth rate only (RO-R, shown in SFig. 3), and 3) seasonal modulation of SST phase transition rate only (RO-F1, shown in SFig. 4). The histograms of phase-locking for RO-T simulation (Figs. 3b,f) are almost the same as that for observations and complete RO simulation (Figs. 3a,e), indicating that phaselocking is primarily attributed by the seasonal modulations of SST growth rate (R) and phase transition rate (F_1) , while the thermocline growth rate (r) and phase transition rate (F_1) contribute little to phase-locking.

In observations the effect of F_1 on phase-locking (Fig. 3d) is much smaller compared to the effect of R (Fig. 3c). This implies that ENSO's phase-locking is mainly dominated by the seasonal modulation of R in observations (Stein et al. 2010, 2014; Chen and Jin 2020). However, in most climate models, the seasonal modulation of F_1 is larger than that in observations and the maximum of F_1 appears in June, resulting in the appearance of the preferred peak month of the histogram associated with the modulation of SST phase transition rate during boreal springtime (Fig. 3h and SFig. 4). The fact that the effect of F_1 is equal or greater (Fig. 3h and SFig. 4) than the effect of R(Fig. 3g and SFig. 3) in most climate models suggests that ENSO phase-locking is codetermined by the seasonal modulations of R and F_1 . That is to say, in some climate models, their winter peak phase-locking is induced by the strong seasonal modulation of SST phase transition rate (F_1) with unrealistic SST growth rate modulation (R). The joint effects of the SST

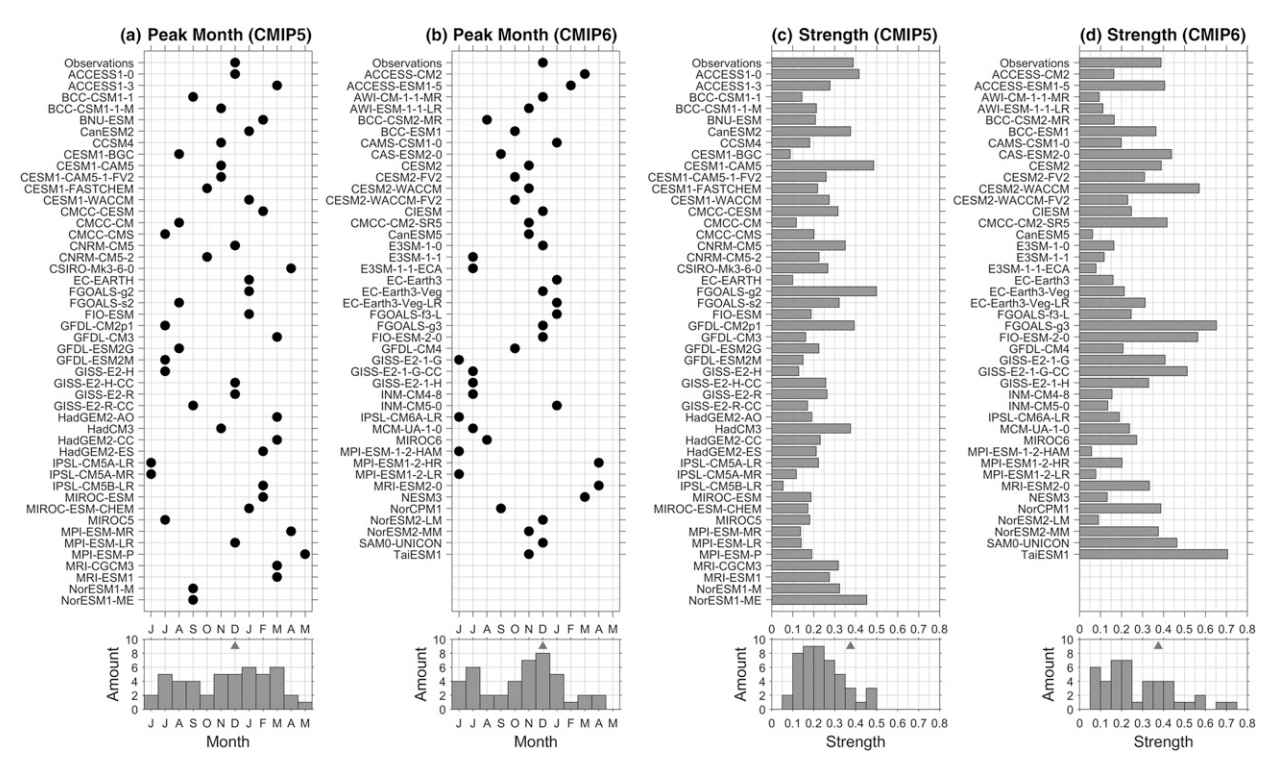


FIG. 2. (top) Preferred peak month of phase-locking for (a) CMIP5 and (b) CMIP6, and the strength of phase-locking preference for (c) CMIP5 and (d) CMIP6. (bottom) The number of models for different peak month or strength. The observed peak month and strength are indicated as triangle marker in the bottom panels.

growth and phase transition rates will be discussed later (see section 5b).

4. A linear dynamics of ENSO phase-locking in CMIP models

In this section, two basic metrics based on the peak phase histogram for all El Niño and La Niña events are used to

evaluate ENSO's phase-locking characteristics in climate models. First, all 90 models are divided into two groups according to the preferred peak month of the histogram φ_p (Figs. 2a,b). One group has preferred peaks in boreal winter (November–January) and another group peaks in other seasons. Next, these groups are subdivided into three subgroups based on the strength of ENSO phase-locking preference φ_s (Figs. 2c,d). Strong phase-locking subgroups are defined as

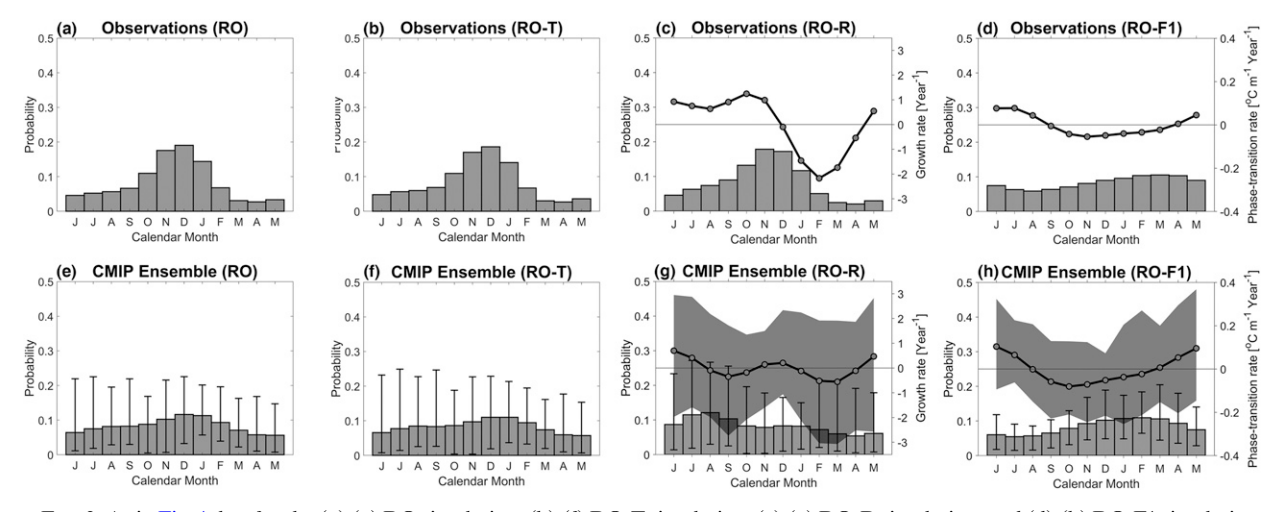


FIG. 3. As in Fig. 1, but for the (a),(e) RO simulation, (b),(f) RO-T simulation, (c),(g) RO-R simulation, and (d),(h) RO-F1 simulation. The curves with dots indicate the SST growth rate in (c) and (g) and SST phase transition rate in (d) and (h). The vertical lines and shading indicate the minimum and maximum values of the histogram and growth rate/phase transition rate, respectively. The mean of SST growth rate and phase transition rate are removed.

TABLE 2. List of CMIP models for strong winter peak phase-locking with appropriate dynamics (Win-S-AD), medium winter peak phase-locking with appropriate dynamics (Win-M-AD), strong winter peak phase-locking with biased dynamics (Win-S-BD), and medium winter peak phase-locking with biased dynamics (Win-M-BD). The numbers in parentheses correspond to the model numbers in Table 1.

	Group					
	Win-S-AD	Win-M-AD	Win-S-BD	Win-M-BD		
Models	(1) ACCESS1.0	(39) MIROC-ESM-CHEM	(6) CanESM2	(4) BCC-CSM1.1-M		
	(16) CNRM-CM5	(54) CAMS-CSM1-0	(9) CESM1-CAM5	(7) CCSM4		
	(20) FGOALS-g2	(67) EC-Earth3-Veg	(56) CESM2	(10) CESM1-CAM5-1-FV2		
	(32) HadCM3	(68) EC-Earth3-Veg-LR	(58) CESM2-WACCM	(12) CESM1-WACCM		
	(70) FGOALS-g3	. ,	(61) CMCC-CM2-SR5	(22) FIO-ESM		
	(89) SAM0-UNICON		(71) FIO-ESM-2-0	(28) GISS-E2-H-CC		
	, ,		(88) NorESM2-MM	(29) GISS-E2-R		
			(90) TaiESM1	(60) CIESM		
				(63) E3SM-1.0		
				(69) FGOALS-f3-L		

having strengths larger than 0.35. Medium and weak phase-locking subgroups have strengths between 0.15 and 0.35 and strengths smaller than 0.15, respectively. According to the above grouping conditions, 34% of CMIP5 models (16 models out of 47) and 47% of CMIP6 models (20 models out of 43) simulate ENSO peaking in boreal winter. In this group of models, about 40% of models (6 models out of 16 CMIP5 models, and 8 models out of 20 CMIP6 models) have the same phase-locking strengths as observations (strong phase-locking subgroup). Only about 15% of climate models simulated observed winter ENSO phase-locking with realistic strengths and the performance of the CMIP6 models (19%) in simulating the strong winter peak ENSO phase-locking is better than the CMIP5 models (13%).

Nevertheless, as mentioned in previous results, in most climate models, the influence of the SST phase transition rate F_1 is more robust than that of SST growth rate R, which means that the determining dynamics of phase-locking differs from observations. Therefore, the contributions of R and F_1 in phase-locking should also be considered as an evaluation condition. In the winter peak phase-locking group, the models that exhibit a significant change in seasonal modulation of R from positive to negative during boreal wintertime will be classified as the winter peak phase-locking group with appropriate dynamics, and the others are called the winter peak phase-locking group with biased dynamics. This classification is also verified through RO-R simulation (SFig. 3), in which the preferred histogram peak of RO-R simulation should appear in boreal wintertime (November-January), meaning that the winter peak phase-locking is mainly attributed by the SST growth rate. According to the above analysis, in the group which simulates winter peak ENSO phase-locking with realistic strengths, only six models have the appropriate dynamics. Therefore, on the basis of the two basic metrics for the ENSO phase-locking together with the natures of seasonal modulations of ENSO's SST growth and phase transition rates from derived linear RO dynamics, CMIP5 and CMIP6 models with winter peak phase-locking are classified into four groups: 1) strong winter peak phase-locking with appropriate dynamics (Win-S-AD), 2) medium winter peak phase-locking with appropriate dynamics (Win-M-AD), 3) strong winter peak phase-locking with biased dynamics (Win-S-BD), and 4) medium winter peak phase-locking with biased dynamics (Win-M-BD). The models of these four groups are listed in Table 2 and the ensemble means of its peak phase histogram are shown in Figs. 4 and 5.

Both the strong and medium winter peak phase-locking with appropriate dynamics groups (Win-S-AD and Win-M-AD) have a significant transition of seasonal modulation of R from positive to negative in boreal wintertime (Fig. 4). However, for the Win-S-AD (Fig. 4a), the seasonal modulation of R (curves with dots in Fig. 4b) is dominated by the annual cycle and the semiannual component is much smaller. In contrast, for the Win-M-AD (Fig. 4d), the modulation of R(curves with dots in Fig. 4e) has a robust semiannual cycle compared to Win-S-AD, leading to the weaker strength for phase-locking. To further discuss the contributions of SST growth and phase transition rates, the ensemble means of RO-R and RO-F1 simulations for Win-S-AD and Win-M-AD are adopted here. For RO-R simulation (Figs. 4b,e), the peak month of the histogram is also in wintertime, which means that the preferred calendar month of phase-locking in Win-S-AD and Win-M-AD are mainly attributed by ENSO's SST growth rate. The influence of SST phase transition rate modulation is less than that of the SST growth rate, but it can increase the strength of phase-locking (Figs. 4c,f). The larger contribution of SST phase transition rates in Win-S-AD than in Win-M-AD is another reason why ENSO phase-locking in Win-S-AD is stronger.

For the winter peak phase-locking groups in biased dynamics (Win-S-BD and Win-M-BD), although their histogram is similar to the appropriate dynamics groups, there is no significant transition of seasonal modulation of R during boreal winter (curves with dots in Figs. 5b,e). The effect of R (RO-R simulation) is more inclined to lock the ENSO peak in July–September (Figs. 5b,e), and the effect of F_1 prefers the peak of histogram occurring in January–March (Figs. 5c,f). For the models in these groups, F_1 has a more considerable influence and its phase-locking is codetermined by the SST growth and phase transition rates, which causes ENSO to phase-lock in

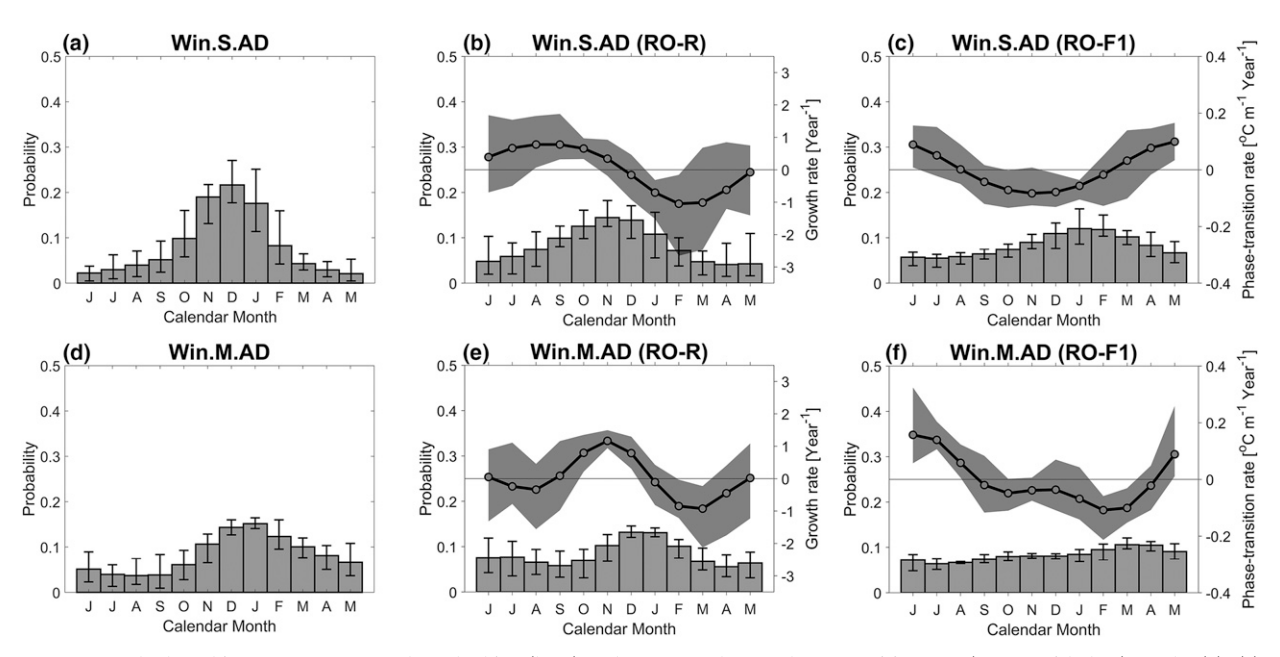


FIG. 4. Peak phase histogram of ENSO phase-locking (bars) and SST growth rate/phase transition rate (curves with dots) for the (a)–(c) Win-S-AD group and (d)–(f) Win-M-AD group, where (b) and (e) are the RO-R simulation and (c) and (f) are the RO-F1 simulation. The vertical lines and shading indicate the minimum and maximum values of the histogram and growth rate/phase transition rate, respectively. The mean of SST growth rate and phase transition rate are removed.

boreal winter. Unlike RO-R simulation of Win-S-AD and Win-M-AD, the histogram amplitude of RO-R simulation in Win-S-BD is smaller than that in Win-M-BD. This is because the phase-locking strengths in these two groups are mainly determined by the joint effects of SST growth and phase transition rates, not just the SST growth rate. The details of this process will be discussed in the next section.

To investigate why some CMIP models reach their peaks in other seasons rather than in boreal winter, the histograms of these groups without preferred peaks φ_p in wintertime are shown in Fig. 6. The preferred peak of phase-locking in February–April (Fig. 6a), May–July (Fig. 6d), and August–October (Fig. 6g) showed their transition of seasonal modulation of R from positive to negative in the corresponding

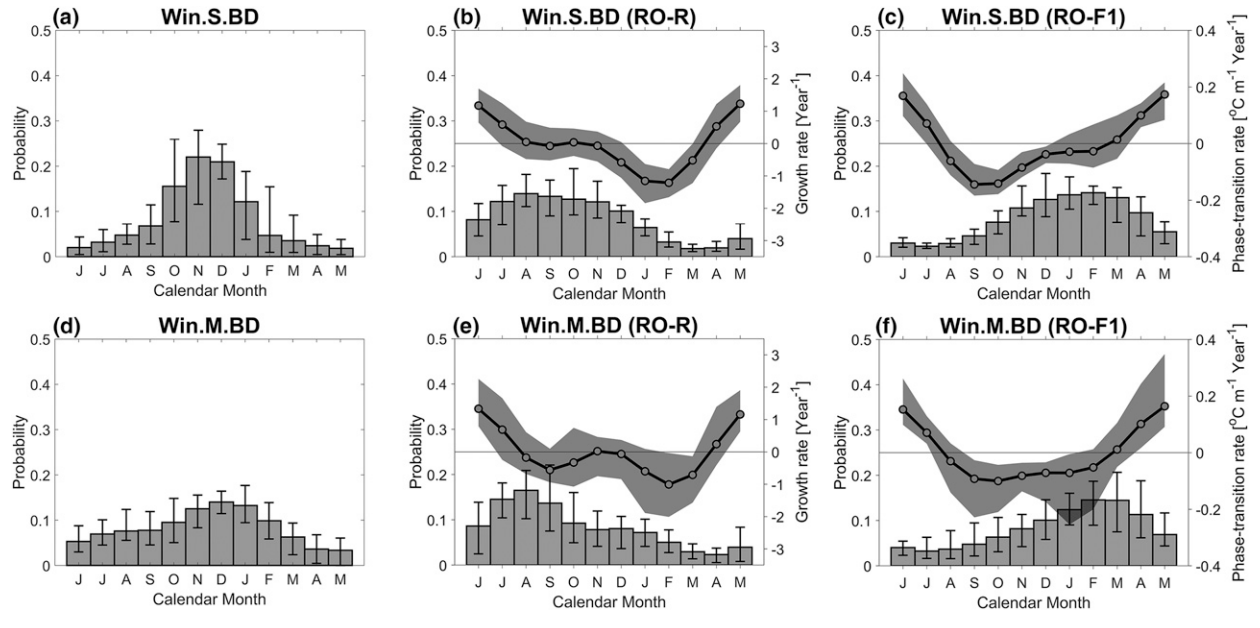


FIG. 5. As in Fig. 4, but for the (a)–(c) Win-S-BD group and (d)–(f) Win-M-BD group.

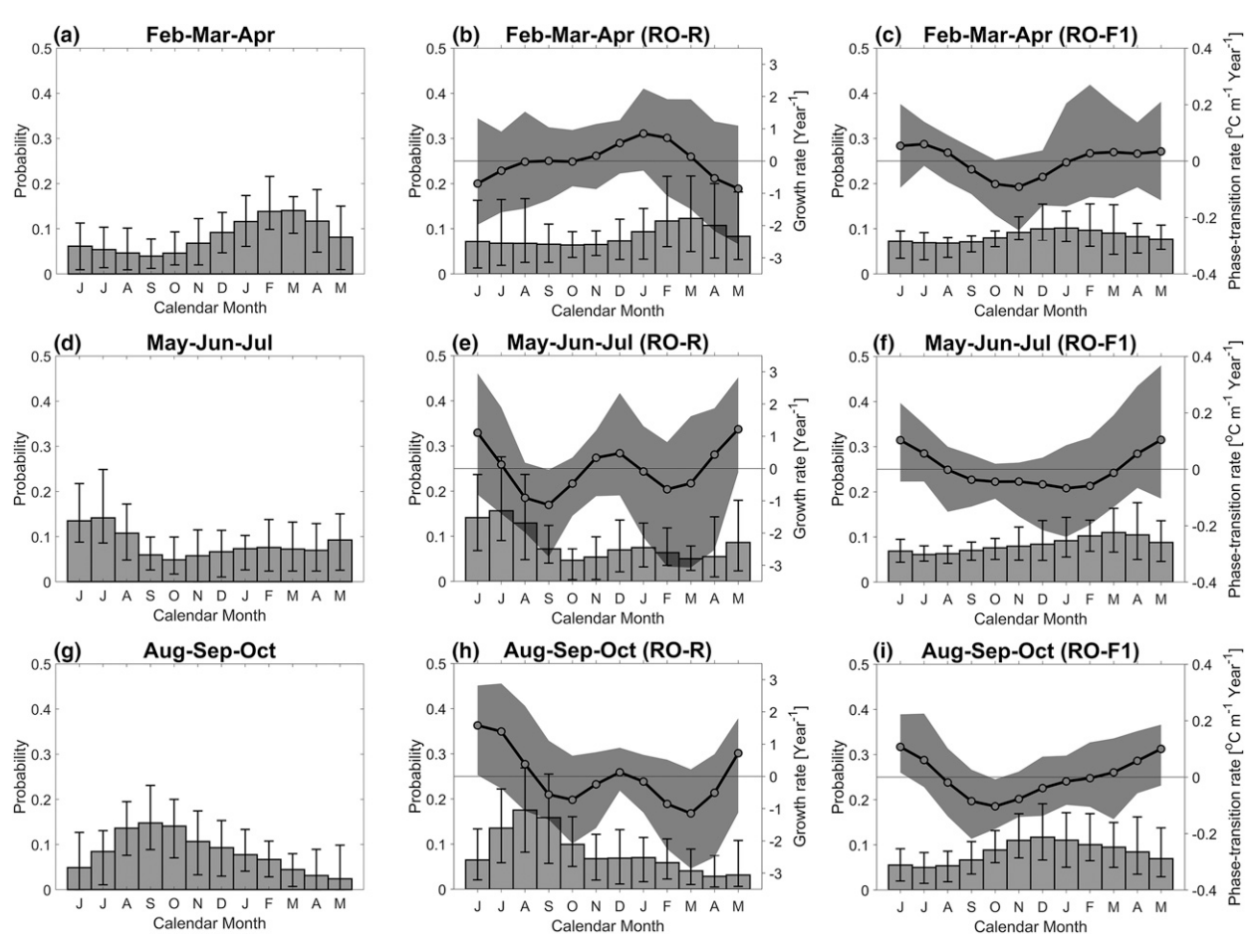


FIG. 6. As in Fig. 4, but for the (a)-(c) February-April, (d)-(f) May-July, and (d)-(f) August-October groups.

season (curves with dots in Figs. 6b,e,h). It is worth noting that the histogram of RO-R simulation in the August–October peak group (Fig. 6h) is similar to the RO-R simulation histogram of the Win-S-BD and Win-M-BD groups (Figs. 5b,e), where the peak of the histogram appears in August. However, the influence of phase transition rates F_1 in the August–October peak group is relatively small (Fig. 6i), and it cannot be combined with SST growth rate R to make the preferred peaks occur in wintertime, such as the Win-S-BD and Win-M-BD groups.

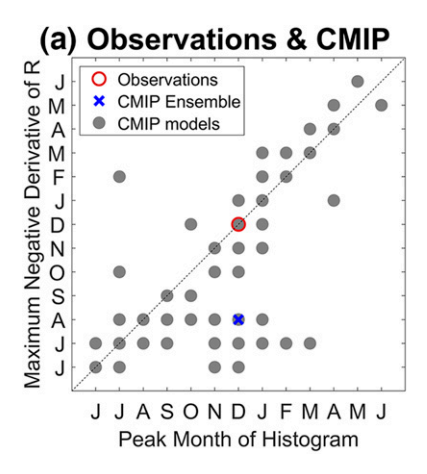
In summary, in the winter peak phase-locking with appropriate dynamics groups (Win-S-AD and Win-M-AD), phase-locking is mainly attributed by the seasonal modulation of R, and F_1 contributes little to the phase-locking, which is similar to observations. In contrast, in the winter peak phase-locking with biased dynamics groups (Win-S-BD and Win-M-BD), the modulation of R does not regulate ENSO to phase-lock in boreal winter, and the winter phase-locking is caused by the combined effect of R and F_1 . Note that an excessively strong semiannual cycle of R tends to reduce the strength of phase-locking or yield unrealistic double peaks. The above results reveal four key factors that play important roles in achieving realistic ENSO phase-locking behaviors with the right

dynamics: 1) correct phase of SST growth rate modulation peaking at the fall; 2) large-enough amplitude for the annual cycle in the growth rate; 3) amplitude of semiannual cycle in the growth rate needs to be small; and 4) amplitude of seasonal modulation in SST phase transition rate needs to be small. In the next section, we will use the linear RO model to investigate the effects of SST growth and phase transition rate modulations on ENSO phase-locking behaviors.

5. Sensitivity examination in the ideal RO model

a. The dependence of preferred peak and strength of phaselocking in the RO model

As mentioned previously, in the observations the preferred peak of histogram occurs when the seasonal modulation of SST growth rate transitions from positive to negative. To investigate the determinants of the preferred peak month of the phase-locking in the climate models, the largest negative derivative of R is chosen as the transition point. If the transition of R is not clear due to the semiannual cycle, such as the negative derivative of R has two comparable values, the transition timing is defined by the annual cycle component of R. The



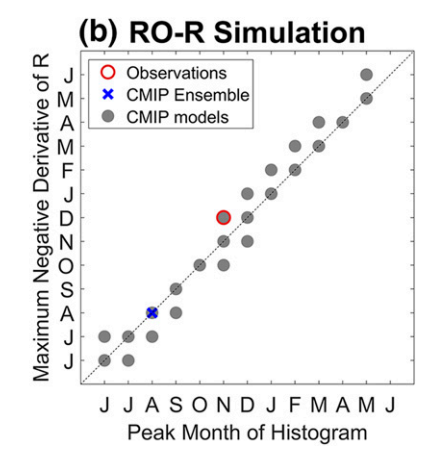


FIG. 7. Scatterplots of the preferred peak month of the histogram and largest negative derivative of the SST growth rate for (a) observations and CMIP models and (b) the RO-R simulation. The gray dots denote the CMIP models. The red circle and blue cross indicate the observations and ensemble mean of CMIP models, respectively.

scatterplot shown in Fig. 7 displays the relationship between the preferred peak month of the histogram and the month of the largest negative derivative of R. In observations, the preferred histogram peak appears at the largest negative derivative of the R (red circle in Fig. 7a); however, they do not entirely follow this rule in the climate models (gray dots in Fig. 7a). In the RO-R simulations that only consider the seasonal modulation in SST growth rate R (Fig. 7b), the preferred histogram peak occurs near the largest negative derivative of R in all climate models, indicating that the influence of F_1 is too strong in most climate models and the preferred peak month of phase-locking is codetermined by the seasonal modulations of both SST growth and phase transition rates.

Using the RO model framework, Chen and Jin (2020) demonstrated that the strength of phase-locking preference is mainly controlled by the mean SST growth rate and its seasonal modulation amplitude. Here, for CMIP models, the strength of ENSO phase-locking preference depends on the amplitude of the mean SST growth rate (R_0) , amplitude of the annual cycle of SST growth rate (R_a) , and amplitude of the annual cycle of SST phase transition rate (F_{1a}) are shown in Fig. 8. There is a positive correlation between the phase-locking strength and R_a (Fig. 8b) as well as between phase-locking strength and R_0 (Fig. 8a). In contrast, the phase-locking strength has little dependence on F_{1a} (Fig. 8c). This small dependence on phaselocking strength in climate models is because all of the influences are combined. If we drop the semiannual component simulated in the climate models (RO-AC simulation; Fig. 8d), the correlation between the phase-locking strength and R_a increases slightly. Further, if we abandon the seasonal modulation of the SST phase transition rate (F_{1a} is set as zero in RO-AC-noF1a simulation; Fig. 8e), this relationship improves dramatically. This suggests that F_{1a} could also affect the strength of phase-locking. Finally, if the mean values of the RO model parameters for each climate models are set to be equal to the observed values (RO-AC-noF1a_obsL0 simulation; Fig. 8f), the phase-locking strength has a good relationship with R_a . The above results reveal that the amplitude of the annual cycle of SST growth rate R_a and mean value of SST growth rate R_0 are crucial for determining the strength of phase-locking preference in the climate models. The seasonal modulation of the phase transition rate F_{1a} also impact the strength of phase-locking, but the effects are much smaller than the seasonal modulation of the SST growth rate or mean SST growth rate.

b. The joint effect of SST growth rate and phase transition rate

In this subsection, sensitivity examinations are conducted using the linear RO model to investigate the joint effects of SST growth and phase transition rates on the two basic ENSO phase-locking metrics. The dependence of the preferred month of phase-locking and the strength of this preference on the annual cycle amplitudes and phases of SST growth rate R and phase transition rate F_1 are examined here. Although the impact of the semiannual component is not negligible in most state-of-the-art climate models, only the annual cycle parts of seasonal modulations are considered for simplicity. In most climate models, because the phase of the SST phase transition rate is similar (SFig. 4), we fix the phase of F_1 , where the maximum appears in June and the minimum occurs in December (Fig. 9). There are no seasonal modulations in the other coefficients of RO model and the mean value of all coefficients is set to the CMIP ensemble mean (The mean values of R, r, F_1 , and F_2 are set to $-0.37 \,\mathrm{yr}^{-1}$, $2.27 \,\mathrm{yr}^{-1}$, $0.14^{\circ}\text{C m}^{-1}\text{yr}^{-1}$, and $28.05 \text{ m}^{\circ}\text{C}^{-1}\text{yr}^{-1}$, respectively).

When considering the dependence of phase-locking strength on R, the annual cycle amplitude of F_1 is set as the ensemble mean of CMIP models $(0.10^{\circ}\text{C m}^{-1}\,\text{yr}^{-1})$. The increase in the ENSO phase-locking strength is a consequence of the increased amplitude of the SST growth rate R_a (Fig. 10a). It is worth noting that the largest strength of phase-locking preference appears when the phase difference between R and F_1 is about 6 months. For the 6-month phase difference, the seasonal evolutions of the SST growth and phase transition rates

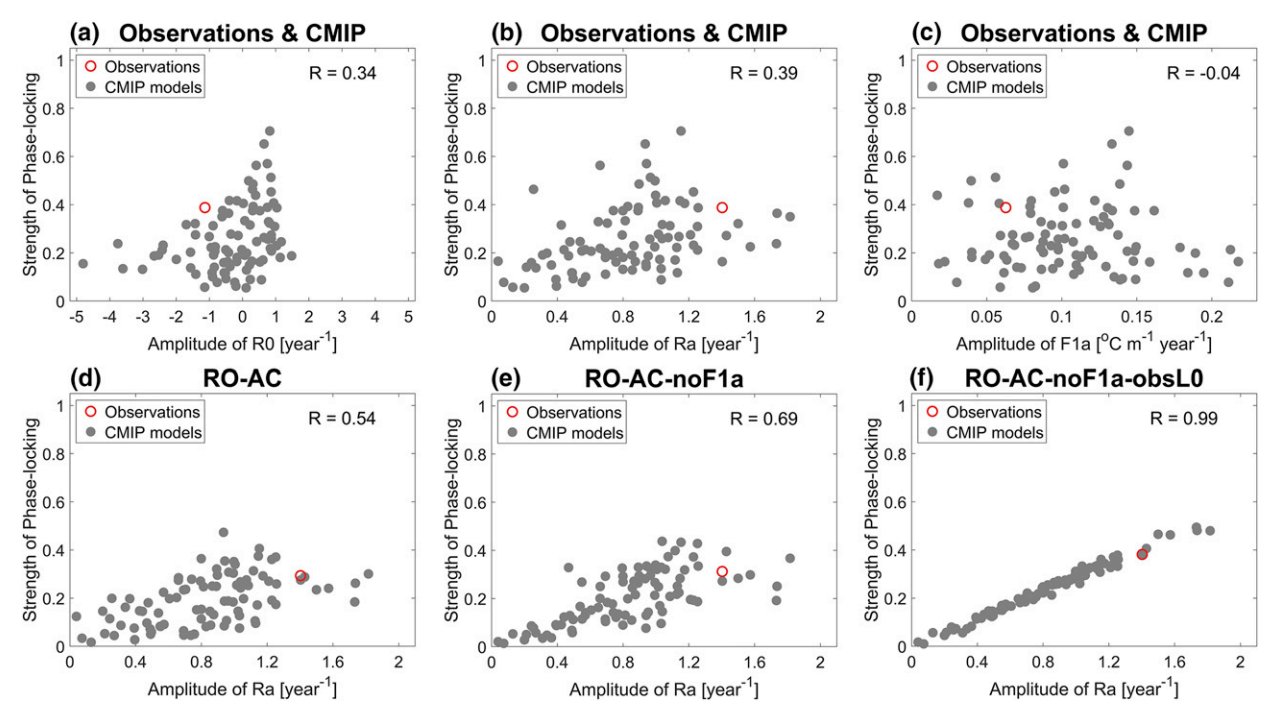


FIG. 8. The strength of ENSO phase-locking preference depends on the (a) amplitude of mean SST growth rate (R_0) , (b) amplitude of the seasonal modulation of SST growth rate (R_a) , and (c) amplitude of the seasonal modulation of SST phase transition rate (F_{1a}) . (d)–(f) The dependence of phase-locking strength on the amplitude of the seasonal modulation of SST growth rate for the RO-AC, RO-AC-noF1a, and RO-AC-noF1a-obsL0 simulations, respectively. Red circle indicates observations.

are shown in Fig. 9 as a solid green curve and black dashed curve, respectively. The preferred peak months of the histogram due to the independent effect of R and F_1 are indicated as triangle markers in Fig. 9. The peak of the histogram caused by the SST growth rate appears when the seasonal modulation of R transitions from positive to negative, while the preferred histogram peak generated by the SST phase transition rate occurs when the seasonal modulation of F_1 changes from negative to positive. The greater phase-locking strength in 6-month phase difference between R and F_1 is because the influences of SST growth and phase transition rates are superimposed in boreal springtime (Fig. 9).

Further, the annual cycle amplitude of R is fitted to the ensemble mean of CMIP models $(0.84\,\mathrm{yr}^{-1})$ to study the dependence of phase-locking strength on F_1 (Fig. 10b). When seasonal modulation of R and F_1 are out of phase (2–10-month phase difference), the increase in ENSO phase-locking strength is the result of an increase in the amplitude of the SST phase transition rate F_{1a} . However, when R and F_1 are in the same phase (phase difference is 0 to 1 month or 11 months), the strength of phase-locking will decrease as the F_{1a} increases. When R and F_1 are out of phase, the influences of R and F_1 are superimposed (green and black triangle markers in Fig. 9); however, when R and F_1 are in the same phase, the influences of R and F_1 will become out of phase (blue and black triangle markers in Fig. 9) and there will be a counteracting effect.

The dependence of preferred ENSO phase-locking peak on R and F_1 is shown in Figs. 10c and 10d. The preferred peak of

phase-locking only depends on the phase of R if R_a is large enough or F_{1a} is small. For a stronger R_a or smaller F_{1a} , the preferred phase-locking peak is completely determined by ENSO's SST growth rate. The winter preferred peak of the

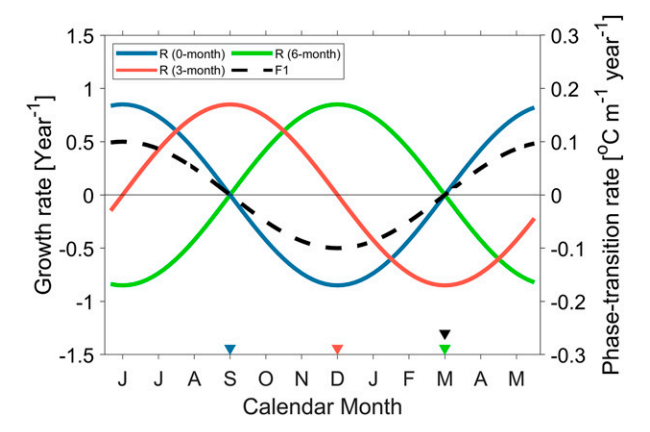


FIG. 9. Schematic diagram for the sensitivity RO examinations. The black dashed curve is the seasonal modulation of the SST phase transition rate. Blue, red, and green curves indicate the seasonal modulations of SST growth rate for 0-, 3-, and 6- phase difference with SST phase transition rate, respectively. The preferred peak months of the histogram due to the independent effect of SST growth rate and phase transition rate are indicated as triangle markers. The mean of SST growth rate and phase transition rate are removed.

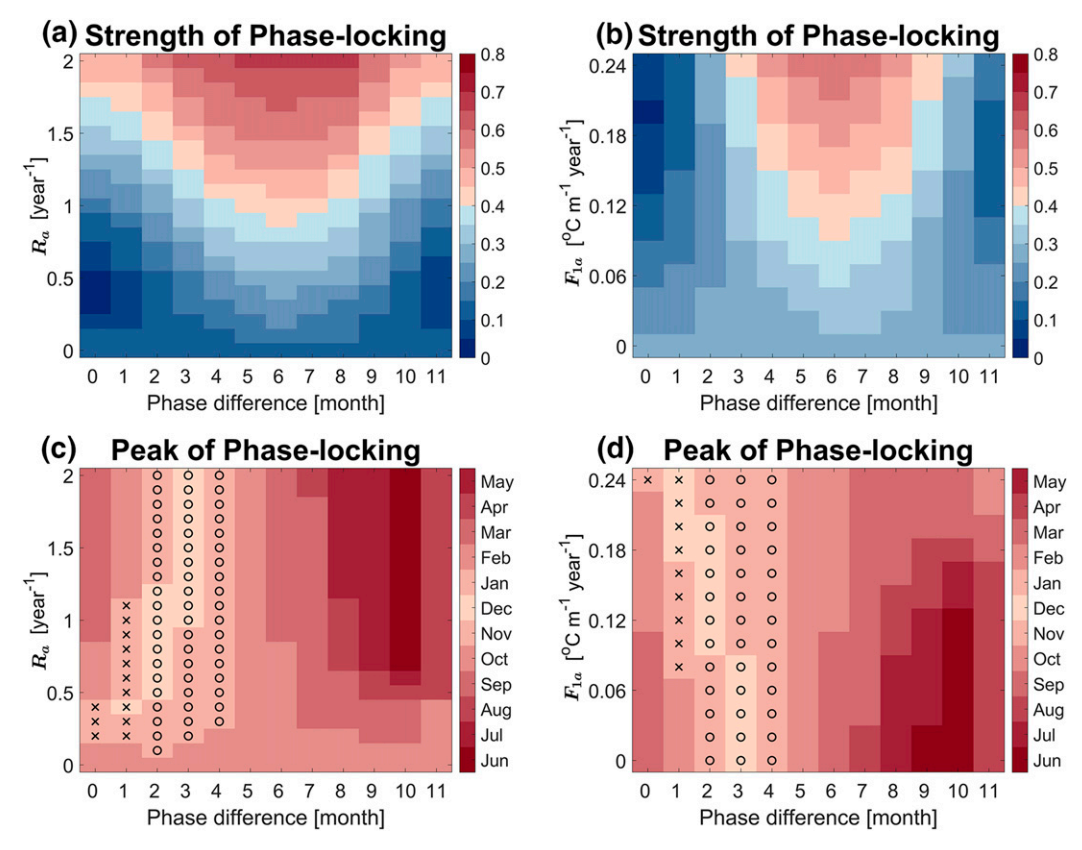


FIG. 10. (top)The strength of ENSO phase-locking preference depends on the phase difference between R and F_1 and the (a) amplitude of the annual cycle of SST growth rate (R_a) and (b) amplitude of the annual cycle of SST phase transition rate (F_{1a}). (bottom) The preferred peak month of phase-locking depends on phase-difference and the (c) amplitude of the annual cycle of SST growth rate (F_{1a}), and (d) amplitude of the annual cycle of SST phase transition rate (F_{1a}). The circles indicate both the preferred peak of the histogram and largest negative derivative of F_{1a} 0 appear in winter. The crosses represent that the winter peak of the histogram appear when the largest negative derivative of F_{1a} 1 does not occur in winter.

histogram appears at the largest negative derivative of R in winter (circle markers in Fig. 10c). However, when the R_a is weak or the F_{1a} is strong enough, the preferred peak of phase-locking depends on the joint effects of seasonal modulation of SST growth rate R and seasonal change of SST phase transition rate F_1 . This means that the winter peak of the histogram may appear when the largest negative derivative of R does not occur in winter (cross markers in Figs. 10c and 9d). The above results can explain why some models (Win-S-BD and Win-M-BD groups) have the largest negative derivative of ENSO's SST growth rate in July-September but the maximum peak of histogram occurs in November–January.

6. Summary and discussion

In this study, the characteristics of ENSO phase-locking in observations and CMIP5 and CMIP6 models are examined based on the 3-month running averaged peak phase histogram. The metric of ENSO phase-locking for the preferred time (φ_p) is defined as the calendar month in which the histogram has its maximum peak. The metric of phase-locking strength (φ_s) is

defined as the relative probability derived from the sum of the 3-month highest values of the histogram centered on φ_p as described in Eq. (9). According to these two basic metrics, the CMIP5 and CMIP6 models performed poorly in simulating the ENSO phase-locking with only about one-third of models simulating ENSO peaking in winter (36 models out of 90). Even in this group of models, only 40% (14 models out of 36) have phase-locking strengths comparable with the observations. Therefore, only about 15% of climate models simulated observed winter ENSO phase-locking with realistic strengths, and the performance of the CMIP6 models (19%) in simulating the strong winter peak ENSO phase-locking is better than the CMIP5 models (13%).

Based on the recharge oscillator model framework, ENSO linear dynamics were derived through the seasonal linear inverse model (sLIM). The phase-locking in observations and CMIP models is shown to be well reproduced by the linear RO model with seasonal modulated dynamics. Our results also suggest that the seasonal modulation of SST growth rate plays a dominant role in controlling ENSO phase-locking in the observations, as argued by previous studies (Stein et al.

2010, 2014; Chen and Jin 2020). In most climate models, in contrast, the seasonal modulations of SST phase transition rate often play an equal or greater role than those of SST growth rate in controlling simulated behaviors of the ENSO phase-locking. As a result, simulated the phase-locking behaviors in climate models are codetermined by both the seasonal modulation of SST growth rate and phase transition rate.

According to the two basic metrics for the ENSO phaselocking, the preferred calendar month of phase-locking and strength of this preference, together with the natures of seasonal modulations of ENSO's SST growth and phase transition rates from derived linear RO dynamics, climate models with winter phase-locking are classified into four groups, namely 1) strong winter peak phase-locking with appropriate dynamics (Win-S-AD); 2) medium winter peak phase-locking with appropriate dynamics (Win-M-AD); 3) strong winter peak phaselocking with biased dynamics (Win-S-BD); and 4) medium winter peak phase-locking with biased dynamics (Win-M-BD). For Win-S-AD and Win-M-AD, phase-locking is mainly controlled by the seasonal modulation of the SST growth rate, which is the same as the observations. In contrast, in Win-S-BD and Win-M-BD, ENSO's phase-locking in boreal winter is caused by the combined effect of SST growth rate and phase transition. An excessively strong semiannual cycle of SST growth rate tends to reduce the phase-locking strength or yield unrealistic double peaks.

Finally, sensitivity examinations are conducted using the linear RO model to investigate the joint effects of SST growth and phase transition rates on the two basic ENSO phase-locking metrics. The preferred calendar month and strength of this preference are found to depend on the combined effects of the amplitudes and phases of SST growth rate and phase transition rate. Our sensitivity study suggests that to simulate ENSO phase-locking by the climate models for the right dynamics, these models must have the four key factors in a tight combination: 1) correct phase of SST growth rate modulation peaking at the fall, 2) largeenough amplitude for the annual cycle in the growth rate, 3) small amplitude of semiannual cycle in the growth rate, and 4) small amplitude of seasonal modulation in SST phase transition rate. For the CMIP5 and CMIP6 models, only six models simulate winter ENSO phase-locking with reasonable amplitudes achieve ENSO phase-locking similar to observations (Win-S-AD group), further indicating the difficulty of climate models to simulate the ENSO phaselocking using the right dynamics.

The knowledge learned from our analysis and understanding gained from ENSO RO dynamics has led us to narrow down the key factors that control the ENSO phase-locking. Nevertheless, how these errors in these factors are related to the biases in climate mean state and its seasonal cycle biases in both coupled and uncoupled physical processes remain to be further delineated. A possible pathway toward addresses these questions is to further decompose ENSO's SST growth and phase transition rates following the approach advocated by Jin et al. (2006, 2020) such that the seasonal modulations of these rates will be explicitly related

to biases in climate mean state and its seasonal cycles as well as the efficiencies of various feedbacks. The modulation of SST growth rate is determined by dynamical damping, thermocline feedback, zonal advective feedback, meridional advective feedback, vertical advective feedback, and thermodynamic damping. The modulation of the SST phase transition rate is controlled by the zonal advective feedback, meridional advective feedback, vertical advective feedback, and thermocline feedback. Further progress along this line of research will be reported in forthcoming papers.

Acknowledgments. The authors thank the three anonymous reviewers for their constructive comments. Han-Ching Chen and Fei-Fei Jin were supported by U.S. NSF Grant AGS-1813611 and Department of Energy Grant DE-SC0005110. We also thank Dr. Andrew T. Wittenberg, Dr. Chung-Hsiung Sui, and Dr. Yu-Heng Tseng for valuable comments and suggestions which have greatly improved the manuscript. We also appreciate SOEST for their editorial support.

Data availability statement. All datasets used in this research can be accessed via the following websites:

HadISST at https://www.metoffice.gov.uk/hadobs/hadisst/; SODAv224 at https://coastwatch.pfeg.noaa.gov/erddap/griddap/hawaii_d90f_20ee_c4cb.html;

CMIP5 at https://esgf-node.llnl.gov/projects/cmip5/; and CMIP6 at https://esgf-node.llnl.gov/projects/cmip6/.

Any other data are available from the corresponding author upon request.

APPENDIX

Seasonal Linear Inverse Model

Considering the following dynamics system:

$$\frac{d\mathbf{X}}{dt} = \mathcal{L}(t)\mathbf{X} + \xi, \tag{A1a}$$

$$\mathcal{L} = \mathcal{L}_0 + \mathcal{L}_a \ . \tag{A1b}$$

Let us consider the following approximation for the linear and annual periodic operator:

$$\mathcal{L}_{a} = \mathcal{L}_{1}^{c} \cos(\omega t) + \mathcal{L}_{1}^{s} \sin(\omega t) + \mathcal{L}_{2}^{c} \cos(2\omega t) + \mathcal{L}_{2}^{s} \sin(2\omega t) + \mathcal{L}_{3}^{s} \cos(3\omega t) + \mathcal{L}_{3}^{s} \sin(3\omega t) + \dots ,$$
(A1c)

where $\omega = 2\pi/(12 \text{ months})$. We further denote the covariance and the annual-harmonic-weighted covariance and their derivatives as

$$C_0 = \langle \mathbf{X}(t) \times \mathbf{X}^T(t - \tau) \rangle, \tag{A2a}$$

$$C_n^c = \langle \cos(n\omega t) \mathbf{X}(t) \times \mathbf{X}^T(t-\tau) \rangle,$$
 (A2b)

$$C_n^s = \langle \sin(n\omega t) \mathbf{X}(t) \times \mathbf{X}^T(t-\tau) \rangle,$$
 (A2c)

$$G_0 = \left\langle \frac{1}{2d} [\mathbf{X}(t+d) - \mathbf{X}(t-d)] \times \mathbf{X}^T(t-\tau) \right\rangle, \quad (A2d)$$

$$G_n^c = \left\langle \frac{\cos(n\omega t)}{2d} \left[\mathbf{X}(t+d) - \mathbf{X}(t-d) \right] \times \mathbf{X}^T(t-\tau) \right\rangle, \quad \text{(A2e)} \qquad G_3^s = \mathcal{L}_0 \times C_3^s + \mathcal{L}_1^c \times \left(\frac{C_4^s + C_2^s}{2} \right) + \mathcal{L}_2^c \times \left(\frac{C_5^s + C_1^s}{2} \right)$$

$$G_n^s = \left\langle \frac{\sin(n\omega t)}{2d} [\mathbf{X}(t+d) - \mathbf{X}(t-d)] \times \mathbf{X}^T(t-\tau) \right\rangle, \quad (A2f)$$

for n = 1, 2, 3, and where τ is the lag time for lag covariance matrix and d is the time step for the central difference. Angle brackets denote an expectation (approximated by averaging in time).

Because the annual cycle is normally smooth and dominated by the first two to three harmonics, we only consider n = 1, 2, 3 here. Then we derive the following equations:

 $G_0 = \mathcal{L}_0 \times C_0^c + \mathcal{L}_1^c \times C_1^c + \mathcal{L}_2^c \times C_2^c + \mathcal{L}_3^c \times C_3^c$

$$(A3a) + \mathcal{L}_{1}^{s} \times C_{1}^{s} + \mathcal{L}_{2}^{s} \times C_{2}^{s} + \mathcal{L}_{3}^{s} \times C_{3}^{s},$$

$$(A3a) + \mathcal{L}_{1}^{s} \times C_{1}^{s} + \mathcal{L}_{2}^{s} \times C_{2}^{s} + \mathcal{L}_{3}^{s} \times C_{3}^{s},$$

$$(A3a) + \mathcal{L}_{1}^{c} \times C_{1}^{c} + \mathcal{L}_{1}^{c} \times \left(\frac{C_{2}^{c} + C_{0}^{c}}{2}\right) + \mathcal{L}_{2}^{c} \times \left(\frac{C_{3}^{c} + C_{1}^{c}}{2}\right)$$

$$+ \mathcal{L}_{3}^{c} \times \left(\frac{C_{4}^{c} + C_{2}^{c}}{2}\right) + \mathcal{L}_{1}^{s} \times \left(\frac{C_{2}^{s} - C_{3}^{s}}{2}\right)$$

$$+ \mathcal{L}_{2}^{s} \times \left(\frac{C_{3}^{s} - C_{-1}^{s}}{2}\right) + \mathcal{L}_{3}^{s} \times \left(\frac{C_{4}^{s} - C_{-2}^{s}}{2}\right),$$

$$(A3b) + \mathcal{L}_{2}^{s} \times \left(\frac{C_{3}^{c} - C_{1}^{c}}{2}\right) + \mathcal{L}_{3}^{s} \times \left(\frac{C_{4}^{s} - C_{-2}^{s}}{2}\right)$$

$$+ \mathcal{L}_{3}^{c} \times \left(\frac{C_{5}^{c} + C_{1}^{c}}{2}\right) + \mathcal{L}_{1}^{s} \times \left(\frac{C_{3}^{s} - C_{1}^{s}}{2}\right)$$

$$+ \mathcal{L}_{2}^{s} \times \left(\frac{C_{3}^{s} - C_{1}^{s}}{2}\right) + \mathcal{L}_{3}^{s} \times \left(\frac{C_{5}^{s} - C_{-1}^{s}}{2}\right),$$

$$+ \mathcal{L}_{2}^{s} \times \left(\frac{C_{4}^{c} - C_{0}^{s}}{2}\right) + \mathcal{L}_{3}^{s} \times \left(\frac{C_{5}^{c} - C_{-1}^{s}}{2}\right)$$

$$+ \mathcal{L}_{2}^{s} \times \left(\frac{C_{5}^{c} + C_{0}^{c}}{2}\right) + \mathcal{L}_{1}^{s} \times \left(\frac{C_{4}^{s} - C_{2}^{s}}{2}\right)$$

$$+ \mathcal{L}_{2}^{s} \times \left(\frac{C_{5}^{c} - C_{1}^{s}}{2}\right) + \mathcal{L}_{3}^{s} \times \left(\frac{C_{5}^{c} - C_{0}^{s}}{2}\right),$$

$$+ \mathcal{L}_{2}^{s} \times \left(\frac{C_{5}^{c} - C_{1}^{c}}{2}\right) + \mathcal{L}_{3}^{s} \times \left(\frac{C_{5}^{c} - C_{0}^{s}}{2}\right),$$

$$+ \mathcal{L}_{3}^{c} \times \left(\frac{C_{4}^{c} + C_{2}^{c}}{2}\right) + \mathcal{L}_{1}^{s} \times \left(\frac{C_{5}^{c} - C_{0}^{s}}{2}\right),$$

$$+ \mathcal{L}_{3}^{c} \times \left(\frac{C_{5}^{c} - C_{1}^{s}}{2}\right) + \mathcal{L}_{1}^{s} \times \left(\frac{C_{5}^{c} - C_{0}^{s}}{2}\right),$$

$$+ \mathcal{L}_{3}^{c} \times \left(\frac{C_{4}^{c} + C_{-2}^{s}}{2}\right) + \mathcal{L}_{1}^{s} \times \left(\frac{C_{5}^{c} - C_{0}^{s}}{2}\right),$$

$$+ \mathcal{L}_{3}^{c} \times \left(\frac{C_{1}^{c} - C_{3}^{c}}{2}\right) + \mathcal{L}_{3}^{s} \times \left(\frac{C_{5}^{c} - C_{2}^{c}}{2}\right),$$

$$+ \mathcal{L}_{2}^{c} \times \left(\frac{C_{1}^{c} - C_{3}^{c}}{2}\right) + \mathcal{L}_{3}^{s} \times \left(\frac{C_{2}^{c} - C_{4}^{c}}{2}\right),$$

$$+ \mathcal{L}_{2}^{s} \times \left(\frac{C_{1}^{c} - C_{3}^{c}}{2}\right) + \mathcal{L}_{3}^{s} \times \left(\frac{C_{2}^{c} - C_{4}^{c}}{2}\right),$$

 $G_2^s = \mathcal{L}_0 \times C_2^s + \mathcal{L}_1^c \times \left(\frac{C_3^s + C_1^s}{2}\right) + \mathcal{L}_2^c \times \left(\frac{C_4^s + C_0^s}{2}\right)$

 $+\mathcal{L}_3^c \times \left(\frac{C_5^s + C_{-1}^s}{2}\right) + \mathcal{L}_1^s \times \left(\frac{C_1^c - C_3^c}{2}\right)$

 $+\mathcal{L}_2^s \times \left(\frac{C_0^c - C_4^c}{2}\right) + \mathcal{L}_3^s \times \left(\frac{C_1^c - C_5^c}{2}\right),$

$$\begin{aligned} G_3^s &= \mathcal{L}_0 \times C_3^s + \mathcal{L}_1^c \times \left(\frac{C_4^s + C_2^s}{2}\right) + \mathcal{L}_2^c \times \left(\frac{C_5^s + C_1^s}{2}\right) \\ &+ \mathcal{L}_3^c \times \left(\frac{C_6^s + C_0^s}{2}\right) + \mathcal{L}_1^s \times \left(\frac{C_2^c - C_4^c}{2}\right) \\ &+ \mathcal{L}_2^s \times \left(\frac{C_1^c - C_5^c}{2}\right) + \mathcal{L}_3^s \times \left(\frac{C_0^c - C_6^c}{2}\right). \end{aligned}$$
(A3g)

Equations (A3b)-(A3g) can be rewritten as

$$G_0 = \mathcal{L}_0 \times C_0^c + \sum_{n=1}^3 (\mathcal{L}_n^c \times C_n^c + \mathcal{L}_n^s \times C_n^s), \tag{A4a}$$

$$G_m^c = \mathcal{L}_0 \times C_m^c + \sum_{n=1}^3 \left[\mathcal{L}_n^c \times \left(\frac{C_{m+n}^c + C_{m-n}^c}{2} \right) + \mathcal{L}_n^s \times \left(\frac{C_{m+n}^s - C_{m-n}^s}{2} \right) \right], \tag{A4b}$$

$$G_m^s = \mathcal{L}_0 \times C_m^s + \sum_{n=1}^3 \left[\mathcal{L}_n^c \times \left(\frac{C_{m+n}^s + C_{m-n}^s}{2} \right) + \mathcal{L}_n^s \times \left(\frac{C_{m-n}^c - C_{m+n}^c}{2} \right) \right].$$
(A4c)

for m=1,2,3. This operator matrix can be solved by using the perturbation method. The solution \mathcal{L} operator is expanded as $\mathcal{L}=\mathcal{L}^{(0)}+\mathcal{L}^{(1)}+\mathcal{L}^{(2)}+\ldots$. We assume that the matrix associated with all components of the harmonics are merely the first-order correction to the \mathcal{L}_0 operator because they are normally significantly smaller than that zeroth order, which is the time-invariant part. Thus, the leading order time-invariant solution is as follows:

$$\mathcal{L}_0^{(0)} = G_0 C_0^{-1}. \tag{A5}$$

The term $\mathcal{L}_0^{(0)}$ is a simple linear operator from the LIM without considering any annual cycle modulation. As we consider all the harmonic-weighted covariance matrices and corresponding derivatives as the first-order quantities comparing with C_0 and G_0 , respectively, and all \mathcal{L}_n^c and \mathcal{L}_n^s as the first-order correction to $\mathcal{L}_0^{(0)}$, then the first-order solution of \mathcal{L}_n^c and \mathcal{L}_n^s can be expressed as

$$\mathcal{L}_n^{c(1)} = 2(G_n^c - \mathcal{L}_0^{(0)} \times C_n^c)C_0^{-1}, \tag{A6a}$$

$$\mathcal{L}_n^{s(1)} = 2(G_n^s - \mathcal{L}_0^{(0)} \times C_n^s)C_0^{-1}.$$
 (A6b)

The second-order correction can be added to the first-order solution as follows:

$$\mathcal{L}_{n}^{c(2)} = -2 \left[\sum_{m=1}^{3} \mathcal{L}_{m}^{c(1)} \times \left(\frac{C_{n+m}^{c} + C_{n-m}^{c}}{2} \right) + \sum_{m=1}^{3} \mathcal{L}_{m}^{s(1)} \times \left(\frac{C_{n+m}^{s} - C_{n-m}^{s}}{2} \right) - \mathcal{L}_{n}^{c(1)} \times \frac{C_{0}}{2} \right] C_{0}^{-1},$$
(A7a)

(A3f)

$$\mathcal{L}_{n}^{s(2)} = -2 \left[\sum_{m=1}^{3} \mathcal{L}_{m}^{c(1)} \times \left(\frac{C_{n+m}^{s} + C_{n-m}^{s}}{2} \right) + \sum_{m=1}^{3} \mathcal{L}_{m}^{s(1)} \times \left(\frac{C_{n-m}^{c} - C_{n+m}^{c}}{2} \right) - \mathcal{L}_{n}^{s(1)} \times \frac{C_{0}}{2} \right] C_{0}^{-1},$$
(A7b)

for n = 1, 2, 3.

The second-order solution that can be added to the leading-order solution for \mathcal{L}_0 is as follows:

$$\mathcal{L}_{0}^{(2)} = -\left[\sum_{n=1}^{3} \left(\mathcal{L}_{n}^{c(1)} \times C_{n}^{c} + \mathcal{L}_{n}^{s(1)} \times C_{n}^{s}\right)\right] C_{0}^{-1}.$$
 (A7c)

Combining the first- and second-order solutions, we will get the annual cycle modulated solution to the second-order accuracy without inverting the whole combined matrix. Note that the solution of the annual-modulated matrix can be solved by whole matrix inversion without the approximation. Interpolated pentad observed temperature and thermocline depth are used to calculate the operator \mathcal{L} in this study. The term τ is set to 1 month (6 pentads) to estimate the first-order operator $\mathcal{L}^{(0)}$ and one pentad to estimate the higher-order operator $\mathcal{L}^{(1)}$ and $\mathcal{L}^{(2)}$. The time step of central difference (d) is one pentad. We ran a number of tests and found that the second-order approximation is highly accurate. This conclusion should hold for climatic application of the method.

REFERENCES

- An, S.-I., and B. Wang, 2001: Mechanisms of locking of the El Niño and La Niña mature phases to boreal winter. *J. Climate*, 14, 2164–2176, https://doi.org/10.1175/1520-0442(2001)014<2164: MOLOTE>2.0.CO:2.
- Battisti, D. S., 1988: Dynamics and thermodynamics of a warming event in a coupled tropical atmosphere–ocean model. J. Atmos. Sci., 45, 2889–2919, https://doi.org/10.1175/1520-0469(1988)045<2889:DATOAW>2.0.CO;2.
- Bellenger, H., E. Guilyardi, J. Leloup, M. Lengaigne, and J. Vialard, 2014: ENSO representation in climate models: From CMIP3 to CMIP5. Climate Dyn., 42, 1999–2018, https://doi.org/10.1007/s00382-013-1783-z.
- Burgers, G., 2005: The simplest ENSO recharge oscillator. Geophys. Res. Lett., 32, L13706, https://doi.org/10.1029/ 2005GL022951.
- —, F.-F. Jin, and G. J. van Oldenborgh, 2005: The simplest ENSO recharge oscillator. *Geophys. Res. Lett.*, 32, L13706, https://doi.org/10.1029/2005GL022951.
- Chen, H. C., and F.-F. Jin, 2020: Fundamental behavior of ENSO phase locking. *J. Climate*, 33, 1953–1968, https://doi.org/ 10.1175/JCLI-D-19-0264.1.
- Eyring, V., S. Bony, G. A. Meehl, C. A. Senior, B. Stevens, R. J. Stouffer, and K. E. Taylor, 2016: Overview of the Coupled Model Intercomparison Project Phase 6 (CMIP6) experimental design and organization. *Geosci. Model Dev.*, 9, 1937–1958, https://doi.org/10.5194/gmd-9-1937-2016.
- Giese, B. S., and S. Ray, 2011: El Niño variability in simple ocean data assimilation (SODA), 1871–2008. J. Geophys. Res., 116, C02024, https://doi.org/10.1029/2010JC006695.
- Ham, Y.-G., and J.-S. Kug, 2014: ENSO phase-locking to the boreal winter in CMIP3 and CMIP5 models. *Climate Dyn.*, 43, 305–318, https://doi.org/10.1007/s00382-014-2064-1.

- —, —, D. Kim, Y. H. Kim, and D. H. Kim, 2013: What controls phase-locking of ENSO to boreal winter in coupled GCMs? *Climate Dyn.*, **40**, 1551–1568, https://doi.org/10.1007/s00382-012-1420-2.
- Hirst, A. C., 1986: Unstable and damped equatorial modes in simple coupled ocean–atmosphere models. *J. Atmos. Sci.*, **43**, 606–632, https://doi.org/10.1175/1520-0469(1986)043<0606: UADEMI>2.0.CO;2.
- Jin, E. K., and J. L. Kinter, 2009: Characteristics of tropical Pacific SST predictability in coupled GCM forecasts using the NCEP CFS. Climate Dyn., 32, 675–691, https://doi.org/10.1007/ s00382-008-0418-2.
- Jin, F.-F., 1997a: An equatorial ocean recharge paradigm for ENSO. Part I: conceptual model. *J. Atmos. Sci.*, **54**, 811–829, https://doi.org/10.1175/1520-0469(1997)054<0811:AEORPF>2.0.CO;2.
- —, 1997b: An equatorial ocean recharge paradigm for ENSO. Part II: A stripped-down coupled model. *J. Atmos. Sci.*, 54, 830–847, https://doi.org/10.1175/1520-0469(1997)054<0830: AEORPF>2.0.CO;2.
- —, J. D. Neelin, and M. Ghil, 1994: El Niño on the devil's staircase: Annual subharmonic steps to chaos. *Science*, 264, 70–72, https://doi.org/10.1126/science.264.5155.70.
- —, S. T. Kim, and L. Bejarano, 2006: A coupled-stability index for ENSO. *Geophys. Res. Lett.*, 33, L23708, https://doi.org/ 10.1029/2006GL027221.
- ——, H.-C. Chen, S. Zhao, M. Hayashi, C. Karamperidou, M. F. Stuecker, R. Xie, and L. Geng, 2020: Simple ENSO models. El Niño Southern Oscillation in a Changing Climate, Geophys. Monogr., Amer. Geophys. Union, 119–151, https://doi.org/10.1002/9781119548164.ch6.
- Joseph, R., and S. Nigam, 2006: ENSO evolution and teleconnections in IPCC's twentieth-century climate simulations: Realistic representation? *J. Climate*, 19, 4360–4377, https://doi.org/10.1175/JCL13846.1.
- Li, T., 1997: Phase transition of the El Niño–Southern Oscillation: A stationary SST mode. J. Atmos. Sci., 54, 2872–2887, https:// doi.org/10.1175/1520-0469(1997)054<2872:PTOTEN>2.0.CO;2.
- Newman, M., P. D. Sardeshmukh, and C. Penland, 2009: How important is air–sea coupling in ENSO and MJO evolution? J. Climate, 22, 2958–2977, https://doi.org/10.1175/2008JCL12659.1.
- —, M. A. Alexander, and J. D. Scott, 2011: An empirical model of tropical ocean dynamics. *Climate Dyn.*, 37, 1823–1841, https://doi.org/10.1007/s00382-011-1034-0.
- Penland, C., and P. D. Sardeshmukh, 1995: The optimal growth of tropical sea surface temperature anomalies. *J. Climate*, 8, 1999–2024, https://doi.org/10.1175/1520-0442(1995)008<1999: TOGOTS>2.0.CO:2.
- Philander, S. G. H., 1983: El Niño Southern Oscillation phenomena. *Nature*, **302**, 295–301, https://doi.org/10.1038/302295a0.
- —, T. Yamagata, and R. C. Pacanowski, 1984: Unstable air–sea interactions in the tropics. *J. Atmos. Sci.*, **41**, 604–613, https://doi.org/10.1175/1520-0469(1984)041<0604:UASIIT>2.0.CO;2.
- Rashid, H. A., and A. C. Hirst, 2016: Investigating the mechanisms of seasonal ENSO phase locking bias in the ACCESS coupled model. *Climate Dyn.*, 46, 1075–1090, https://doi.org/10.1007/ s00382-015-2633-y.
- Rayner, N. A., D. E. Parker, E. B. Horton, C. K. Folland, L. V. Alexander, D. P. Rowell, E. C. Kent, and A. Kaplan, 2003: Global analyses of sea surface temperature, sea ice, and night marine air temperature since the late nineteenth century. J. Geophys. Res., 108, 4407, https://doi.org/10.1029/2002JD002670.
- Stein, K., N. Schneider, A. Timmermann, and F.-F. Jin, 2010: Seasonal synchronization of ENSO events in a linear

- stochastic model. *J. Climate*, **23**, 5629–5643, https://doi.org/10.1175/2010JCLI3292.1.
- —, A. Timmermann, N. Schneider, F.-F. Jin, and M. F. Stuecker, 2014: ENSO seasonal synchronization theory. *J. Climate*, 27, 5285–5310, https://doi.org/10.1175/JCLI-D-13-00525.1.
- Taylor, K. E., R. J. Stouffer, and G. A. Meehl, 2012: An overview of CMIP5 and the experiment design. *Bull. Amer. Meteor. Soc.*, **93**, 485–498, https://doi.org/10.1175/BAMS-D-11-00094.1.
- Tziperman, E., L. Stone, M. A. Cane, and H. Jarosh, 1994: El Niño chaos: Overlapping of resonances between the seasonal cycle and the Pacific Ocean–atmosphere oscillator. *Science*, **264**, 72–74, https://doi.org/10.1126/science.264.5155.72.
- ——, S. E. Zebiak, and M. A. Cane, 1997: Mechanisms of seasonal–ENSO interaction. *J. Atmos. Sci.*, **54**, 61–71, https://doi.org/10.1175/1520-0469(1997)054<0061:MOSEI>2.0.CO;2.

- Vimont, D. J., M. A. Alexander, and M. Newman, 2014: Optimal growth of central and east Pacific ENSO events. *Geophys. Res. Lett.*, 41, 4027–4034, https://doi.org/10.1002/2014GL059997.
- Wengel, C., M. Latif, W. Park, J. Harlaß, and T. Bayr, 2018: Seasonal ENSO phase locking in the Kiel Climate Model: The importance of the equatorial cold sea surface temperature bias. *Climate Dyn.*, **50**, 901–919, https://doi.org/10.1007/s00382-017-3648-3.
- Wittenberg, A. T., A. Rosati, N. C. Lau, and J. J. Ploshay, 2006: GFDL's CM2 global coupled climate models. Part III: Tropical Pacific climate and ENSO. *J. Climate*, **19**, 698–722, https://doi.org/10.1175/JCLI3631.1.
- Zheng, W., and Y. Yu, 2007: ENSO phase-locking in an ocean-atmosphere coupled model FGCM-1.0. *Adv. Atmos. Sci.*, **24**, 833–844, https://doi.org/10.1007/s00376-007-0833-z.